Understanding the effects of Cd- and Ag-doping in Cu₂ZnSnS₄ solar cells

Gopalakrishnan Sai Gautam,[1] Thomas P. Senftle,[1,†] and Emily A. Carter[2]

[1]Department of Mechanical and Aerospace Engineering and [2]School of Engineering and Applied Science, Princeton University, Princeton, NJ 08544-5263, United States
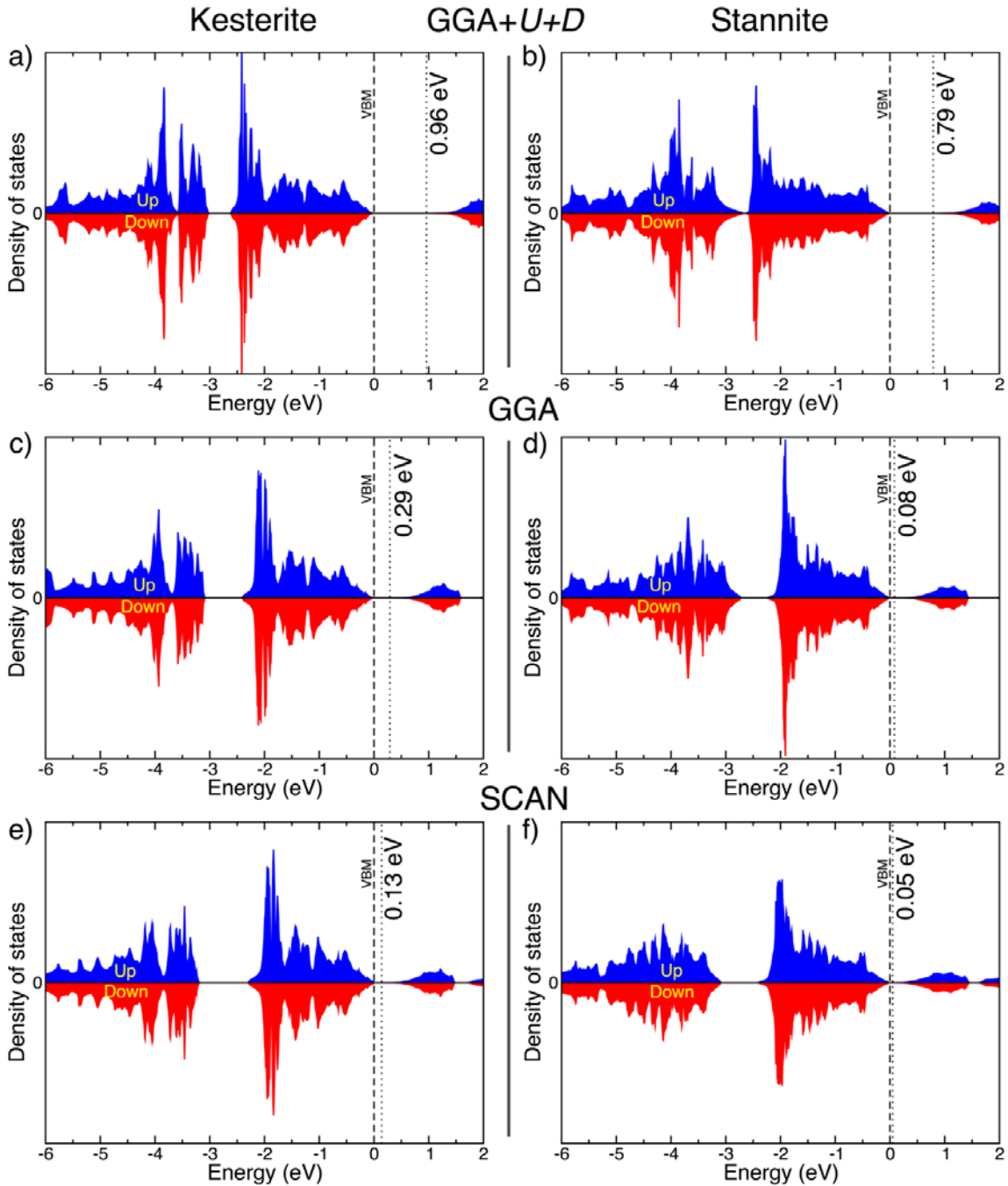[†] Present address: Department of Chemical and Biomolecular Engineering, Rice University, Houston, TX 77005
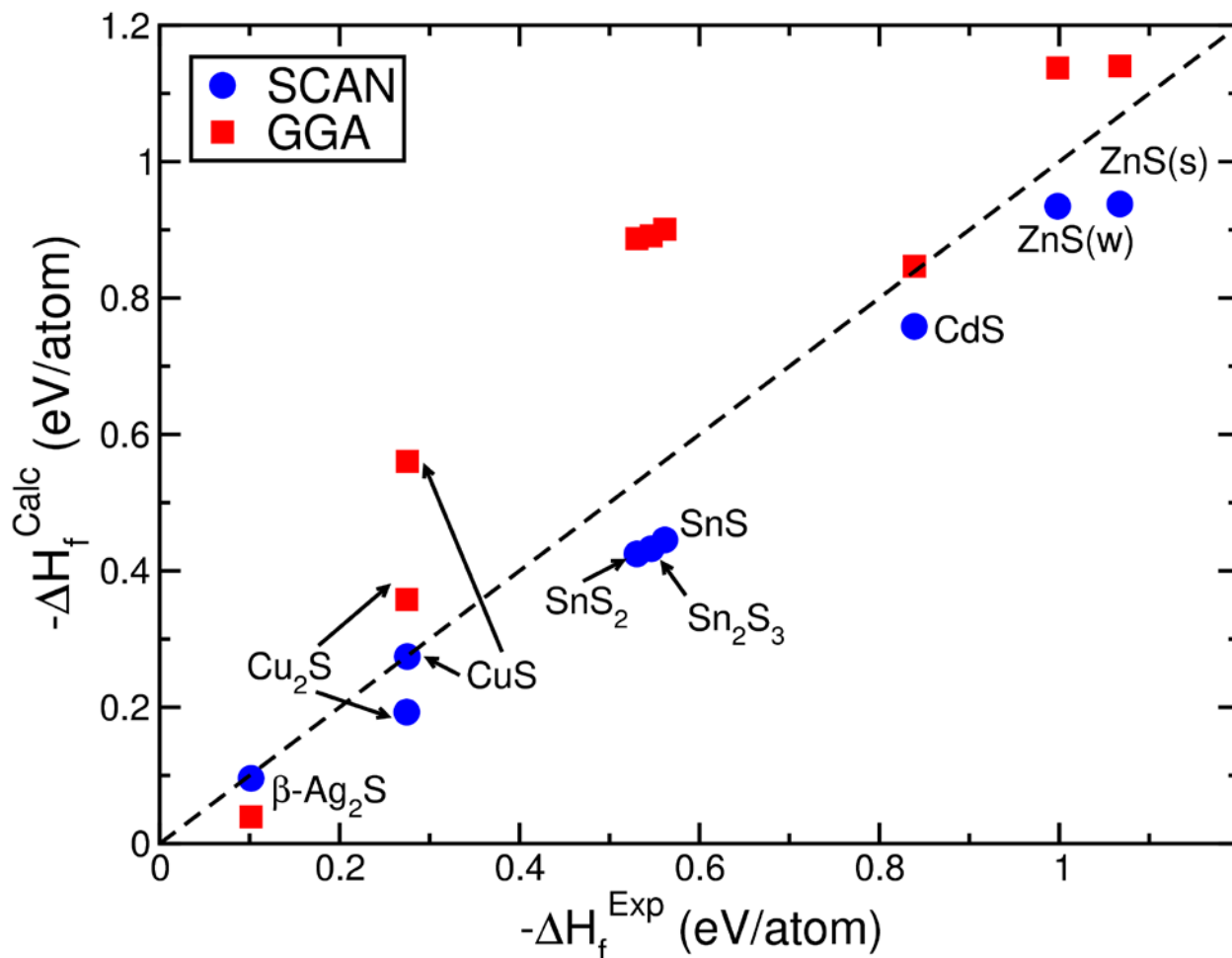
Figure S1: Calculated formation enthalpies of various binary sulfides, using GGA (red squares) and SCAN (blue circles), are benchmarked against the experimental formation enthalpies obtained from Kubaschewski and Wagman tables.[1,2] The GGA and SCAN formation enthalpies here are calculated at 0 K and do not include zero-point energy, entropic, or pressure-volume contributions, which typically cancel during formation enthalpy calculations in solids. The dashed black line indicates equality. Details of the specific structures used in calculating the energies are provided in Table S2. ZnS(w) and ZnS(s) indicate the wurtzite and sphalerite polymorphs of ZnS, respectively. The mean absolute error (MAE) of SCAN in predicting the binary sulfide formation energies is ~ 0.078 eV, significantly lower than the MAE of GGA (~ 0.188 eV), indicating that SCAN describes the energetics of sulfides better than GGA.

Table S1: Comparison of experimental lattice parameters of layered-SnS_2[3] and kesterite-Cu_2ZnSnS_4[4] with theoretical predictions from SCAN, dispersion corrections[5] added to SCAN (SCAN+D), and long-range van der Waals corrections added to SCAN (SCAN+rVV10).[6] While SCAN+D accurately captures the inter-layer spacing of SnS_2, both a and c lattice parameters of Cu_2ZnSnS_4 are predicted with greater accuracy by SCAN, compared to SCAN+D and SCAN+rVV10. Thus, SCAN predicts both formation energies (Figure S1) and lattice parameters in the Cu-Zn-Sn-S system accurately.

Compound	Experiment	SCAN	SCAN+D	SCAN+rVV10
	Lattice parameters (Å)			
SnS_2	$a = 3.64$	$a = 3.67$	$a = 3.65$	$a = 3.66$
	$c = 5.90$	$c = 6.18$	$c = 5.76$	$c = 6.00$
Cu_2ZnSnS_4	$a = 5.43$	$a = 5.40$	$a = 5.31$	$a = 5.39$
	$c = 10.87$	$c = 10.82$	$c = 10.61$	$c = 10.79$

Figure S2: Total density of states for kesterite (left column) and stannite (right column) polymorphs of Cu_2ZnSnS_4, calculated using GGA+U+D (panels a, b), GGA (c, d), and SCAN (e, f), respectively, using structures calculated with each functional. The dashed and dotted black lines in each panel indicate the valence band maximum (VBM) and the conduction band minimum (CBM), respectively. The number adjacent to the CBM in each panel indicates the predicted band (eigenvalue) gap for the given structure and functional. Blue and red shaded regions indicate up and down spin, respectively. The band gaps predicted by SCAN for both kesterite and stannite structures are comparable to GGA predictions, while GGA+U+D compares better with both experimental[7] and higher-level GW calculations.[8] Notably, all three functionals predict a lower band gap for stannite than for kesterite, consistent with experiment.
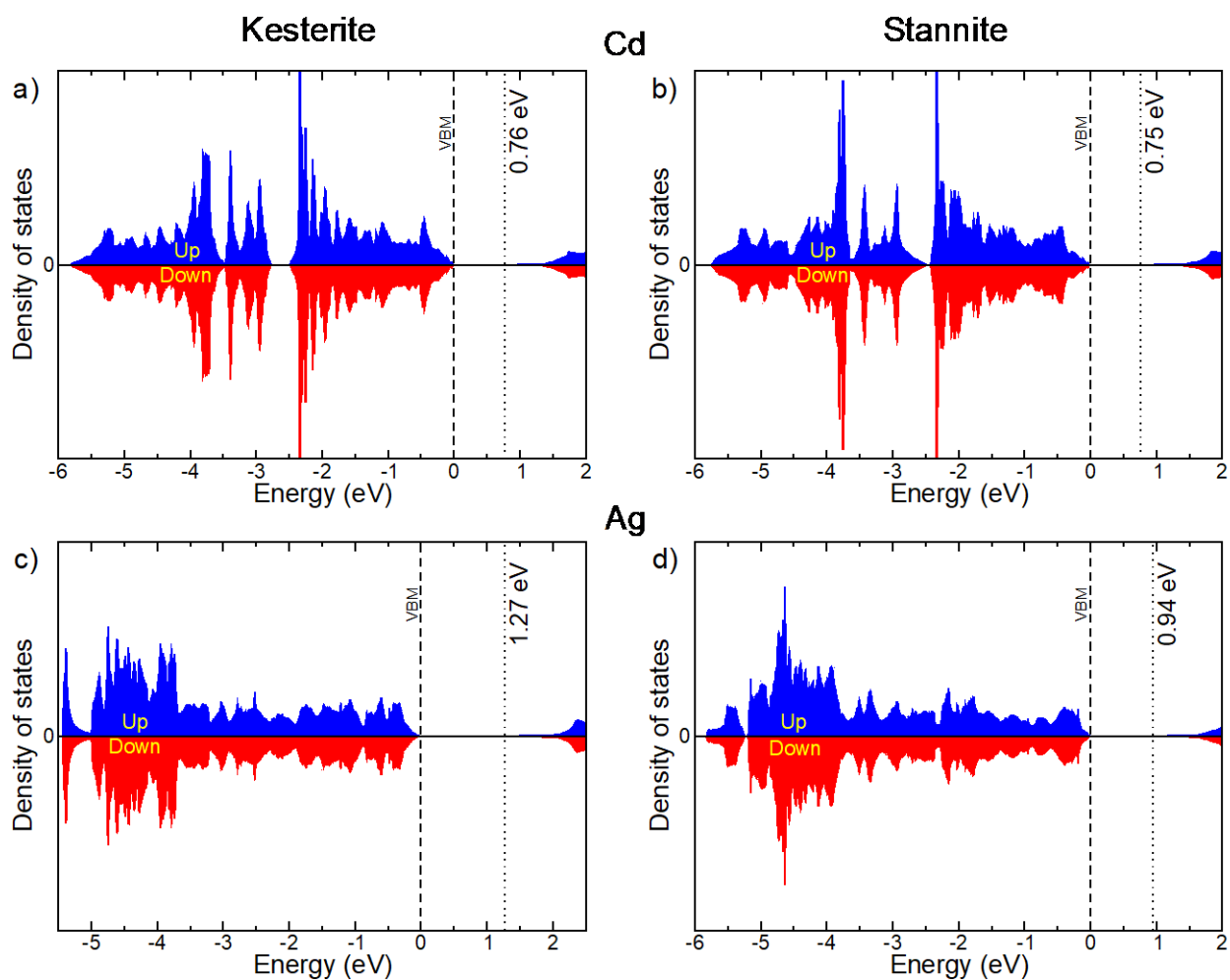
Figure S3: Total density of states (DOS) for kesterite (left column) and stannite (right column) polymorphs of Cu_2CdSnS_4 (panels a and b) and Ag_2ZnSnS_4 (panels c and d). All DOS calculations are done using the GGA+U+D functional (see Methods section in the main text). The dashed and dotted black lines in each panel indicate the valence band maximum (VBM) and the conduction band minimum (CBM), respectively. The number adjacent to the CBM in each panel indicates the predicted band (eigenvalue) gap for the given structure. Blue and red shaded regions indicate up and down spin, respectively. Notably, Cd (Ag) addition to Cu_2ZnSnS_4, via replacement of Zn (Cu), causes the band gap of both the kesterite and stannite polymorphs to decrease (increase) compared to undoped-Cu_2ZnSnS_4.

Table S2: Compositions, space group of the structure used in our calculations, and the corresponding collection code from the inorganic crystal structure database (ICSD)[9] for all phases used in constructing the various phase diagrams (see Methods section in the manuscript and Tables S3, S4, and S5) are listed. For compounds without a corresponding entry in the ICSD, such as kesterite-Cu_2CdSnS_4, we used an analogous structure (kesterite-Cu_2ZnSnS_4) as an initial guess in our DFT-SCAN structure relaxations.

Composition	Space Group	ICSD Collection Code
Elements		
Cu	$Fm\overline{3}m$	43493
Zn	$P6_3/mmc$	247147
Sn	$Fd\overline{3}mS$	53789
S	FdddZ	27261
Cd	$P6_3/mmc$	52264
Ag	$Fm\overline{3}m$	52257
Binaries		
CuS	$P6_3/mmc$	32105
Cu_2S	$P12_1/c1$	23596
Cu_7S_4	Pnma	16011
SnS	Pnma	24376
Sn_2S_3	Pnma	653956
SnS_2	$P\overline{3}m1$	650993
ZnS (wurtzite)	$P6_3mc$	67543
ZnS (sphalerite)	$F\overline{4}3m$	77090
CdS	$P6_3mc$	154186
β-Ag_2S	$P12_1/c1$	182916
Ag_2S	$P12_1/n1$	262632
Ag_2S	$P2_12_12_1$	262634
Ag_8S	Imm2	79770
Ternaries		
Cu_2SnS_3	C1c1	91762
Cu_4SnS_4	Pnma	833
CuAgS	$Cmc2_1$	66580
CuAgS	$Pmc2_1$	66581
CuAgS	P4/nmmZ	251149
Ag_3CuS_2	$I4_1/amdZ$	67526
Ag_3CuS_2	$I4_1/aZ$	163983
$Ag_4Sn_3S_8$	$P4_132$	164431
Ag_8SnS_6	$Pna2_1$	42533
Quaternaries		
Cu_2ZnSnS_4 (stannite)	$I\overline{4}2m$	192110
Cu_2ZnSnS_4 (kesterite)	$I\overline{4}$	628895
Cu_2CdSnS_4 (stannite)	$I\overline{4}2m$	238144
Cu_2CdSnS_4 (kesterite)	$I\overline{4}$	—
Ag_2ZnSnS_4 (stannite)	$I\overline{4}2m$	605734
Ag_2ZnSnS_4 (kesterite)	$I\overline{4}$	—

Quinaries		
$Cu_2Zn_{0.5}Cd_{0.5}SnS_4$ (stannite)	$I\bar{4}2m$	619778
$Cu_2Zn_{0.5}Cd_{0.5}SnS_4$ (kesterite)	$I\bar{4}$	—
$CuAgZnSnS_4$ (stannite)	$I\bar{4}2m$	—
$CuAgZnSnS_4$ (kesterite)	$I\bar{4}$	—

Table S3: Phases in equilibrium with kesterite-Cu_2ZnSnS_4 and the corresponding elemental chemical potentials, as calculated via DFT-SCAN from the 0 K Cu-Zn-Sn-S quaternary phase diagram. Each row indicates a thermodynamic facet, with each facet representing three unique phases that are in equilibrium with Cu_2ZnSnS_4. The first three rows (in bold) correspond to Cu-rich, constrained Cu-poor, and Cu-poor conditions, respectively (see Methods section in main text). Examples of equations used for determining the chemical potentials for each thermodynamic facet are given in Table S6.

Compounds in equilibrium with Cu_2ZnSnS_4	Chemical potential (μ, eV)			
	Cu	Zn	Sn	S
Cu-SnS-ZnS	**0.00**	**-1.12**	**-0.13**	**-0.76**
SnS_2-SnS-ZnS	**-0.38**	**-1.49**	**-0.51**	**-0.38**
S-SnS_2-ZnS	**-0.57**	**-1.88**	**-1.27**	**0.00**
Cu-Cu_7S_4-ZnS	0.00	-1.25	-0.54	-0.62
Cu-Cu_7S_4-Cu_2SnS_3	0.00	-1.35	-0.44	-0.62
Cu-SnS-Cu_2SnS_3	0.00	-1.26	-0.18	-0.71
CuS-Cu_7S_4-ZnS	-0.10	-1.43	-0.86	-0.45
CuS-Cu_7S_4-Cu_2SnS_3	-0.10	-1.52	-0.77	-0.45
SnS_2-SnS-Cu_2SnS_3	-0.33	-1.59	-0.51	-0.38
SnS_2-CuS-Cu_2SnS_3	-0.49	-1.91	-1.16	-0.06
S-CuS-ZnS	-0.55	-1.88	-1.31	0.00
S-SnS_2-CuS	-0.55	-1.91	-1.27	0.00

Table S4: Phases in equilibrium with kesterite-Cu_2ZnSnS_4 and the corresponding elemental chemical potentials, as calculated via DFT-SCAN from the 0 K Cu-Zn-Sn-S-Cd quinary phase diagram. Each row indicates a thermodynamic facet, with each facet representing four unique phases that are in equilibrium with Cu_2ZnSnS_4. The first three rows (in bold) correspond to Cu-rich, constrained Cu-poor, and Cu-poor conditions, respectively (see Methods section in main text). Examples of equations used for determining the chemical potentials for each thermodynamic facet are given in Table S6.

Compounds in equilibrium with Cu_2ZnSnS_4	Chemical potential (μ, eV)				
	Cu	Zn	Sn	S	Cd
Cu-SnS-ZnS-CdS	**0.00**	**-1.12**	**-0.13**	**-0.76**	**-0.76**
SnS_2-SnS-ZnS-CdS	**-0.38**	**-1.49**	**-0.51**	**-0.38**	**-1.13**
S-SnS_2-ZnS-CdS	**-0.57**	**-1.88**	**-1.27**	**0.00**	**-1.52**
S-CuS-ZnS-CdS	-0.55	-1.88	-1.31	0.00	-1.52
CuS-Cu_7S_4-ZnS-CdS	-0.10	-1.43	-0.86	-0.45	-1.07
Cu-Cu_7S_4-ZnS-CdS	0.00	-1.25	-0.54	-0.62	-0.89
S-CuS-SnS_2-Cu_2CdSnS_4	-0.55	-1.91	-1.27	0.00	-1.53
S-CuS-CdS-Cu_2CdSnS_4	-0.55	-1.90	-1.29	0.00	-1.52
S-SnS_2-CdS-Cu_2CdSnS_4	-0.56	-1.90	-1.27	0.00	-1.52
SnS_2-SnS-CdS-Cu_2CdSnS_4	-0.36	-1.52	-0.51	-0.38	-1.13
CuS-Cu_7S_4-CdS-Cu_2CdSnS_4	-0.10	-1.45	-0.84	-0.45	-1.07
Cu-SnS-CdS-Cu_2CdSnS_4	0.00	-1.15	-0.14	-0.75	-0.77
Cu-Cu_7S_4-CdS-Cu_2CdSnS_4	0.00	-1.28	-0.52	-0.62	-0.89
SnS_2-SnS-Cu_2SnS_3-Cu_2CdSnS_4	-0.33	-1.59	-0.51	-0.38	-1.20
SnS_2-CuS-Cu_2SnS_3-Cu_2CdSnS_4	-0.49	-1.91	-1.16	-0.06	-1.53
CuS-Cu_7S_4-Cu_2SnS_3-Cu_2CdSnS_4	-0.10	-1.52	-0.77	-0.45	-1.14
Cu-SnS-Cu_2SnS_3-Cu_2CdSnS_4	0.00	-1.26	-0.18	-0.71	-0.88
Cu-Cu_7S_4-Cu_2SnS_3-Cu_2CdSnS_4	0.00	-1.35	-0.45	-0.62	-0.97

Table S5: Phases in equilibrium with kesterite-Cu_2ZnSnS_4 and the corresponding elemental chemical potentials, as calculated via DFT-SCAN from the 0 K Cu-Zn-Sn-S-Ag quinary phase diagram. Each row indicates a thermodynamic facet, with each facet representing four unique phases that are in equilibrium with Cu_2ZnSnS_4. The first three rows (in bold) correspond to Cu-rich, constrained Cu-poor, and Cu-poor conditions, respectively (see Methods section in main text). Examples of equations used for determining the chemical potentials for each thermodynamic facet are given in Table S6.

Compounds in equilibrium with Cu_2ZnSnS_4	Chemical potential (μ, eV)				
	Cu	Zn	Sn	S	Ag
Cu-SnS-ZnS-Ag	**0.00**	**-1.12**	**-0.13**	**-0.76**	**0.00**
SnS-ZnS-Ag$_2$ZnSnS$_4$-Ag	**-0.34**	**-1.46**	**-0.47**	**-0.42**	**0.00**
S-SnS$_2$-ZnS-Ag$_2$ZnSnS$_4$	**-0.57**	**-1.88**	**-1.27**	**0.00**	**-0.23**
Cu-Cu$_7$S$_4$-ZnS-Ag	0.00	-1.25	-0.54	-0.62	0.00
CuS-Cu$_7$S$_4$-ZnS-Ag	-0.10	-1.43	-0.86	-0.45	0.00
CuS-ZnS-Ag$_2$S-Ag	-0.26	-1.59	-1.03	-0.29	0.00
ZnS-Ag$_8$SnS$_6$-Ag$_2$ZnSnS$_4$-Ag	-0.34	-1.59	-0.85	-0.29	0.00
SnS$_2$-SnS-ZnS-Ag$_2$ZnSnS$_4$	-0.38	-1.49	-0.51	-0.38	-0.03
ZnS-Ag$_2$S-Ag$_8$SnS$_6$-Ag	-0.34	-1.59	-0.87	-0.29	0.00
CuS-ZnS-Ag$_2$S-Ag$_8$SnS$_6$	-0.41	-1.74	-1.18	-0.13	-0.08
CuS-ZnS-Ag$_8$SnS$_6$-Ag$_2$ZnSnS$_4$	-0.43	-1.75	-1.19	-0.12	-0.08
S-CuS-ZnS-Ag$_2$ZnSnS$_4$	-0.55	-1.88	-1.31	0.00	-0.21
Cu-Cu$_7$S$_4$-Cu$_2$SnS$_3$-Ag	0.00	-1.35	-0.44	-0.62	0.00
Cu-SnS-Cu$_2$SnS$_3$-Ag	0.00	-1.26	-0.18	-0.71	0.00
CuS-Cu$_7$S$_4$-Cu$_2$SnS$_3$-Ag	-0.10	-1.52	-0.77	-0.45	0.00
CuS-Cu$_2$SnS$_3$-Ag$_2$S-Ag	-0.26	-1.68	-0.93	-0.29	0.00
Cu$_2$SnS$_3$-Ag$_8$SnS$_6$-Ag$_2$ZnSnS$_4$-Ag	-0.34	-1.65	-0.66	-0.32	0.00
SnS-SnS$_2$-Ag$_2$ZnSnS$_4$-Ag	-0.34	-1.56	-0.51	-0.38	0.00
SnS-SnS$_2$-Cu$_2$SnS$_3$-Ag	-0.33	-1.59	-0.51	-0.38	0.00
SnS$_2$-Cu$_2$SnS$_3$-Ag$_2$ZnSnS$_4$-Ag	-0.34	-1.62	-0.56	-0.36	0.00
Cu$_2$SnS$_3$-Ag$_2$S-Ag$_8$SnS$_6$-Ag	-0.29	-1.68	-0.87	-0.29	0.00
CuS-Cu$_2$SnS$_3$-Ag$_2$S-Ag$_8$SnS$_6$	-0.32	-1.74	-0.99	-0.23	-0.03
CuS-Cu$_2$SnS$_3$-Ag$_8$SnS$_6$-Ag$_2$ZnSnS$_4$	-0.46	-1.88	-1.13	-0.09	-0.12
CuS-SnS$_2$-Cu$_2$SnS$_3$-Ag$_2$ZnSnS$_4$	-0.49	-1.91	-1.16	-0.06	-0.15
S-CuS-SnS$_2$-Ag$_2$ZnSnS$_4$	-0.55	-1.91	-1.27	0.00	-0.21

Table S6: Equations detailing the constraints that determine the various chemical conditions, as detailed in the manuscript.

Condition	Constraints
Cu-rich	$\Delta G_f^{Cu_2ZnSnS_4} = 2\mu_{Cu} + \mu_{Zn} + \mu_{Sn} + 4\mu_S$ $\mu_{Cu} = \mu_{Cu}^{metal} \equiv 0$ $\Delta G_f^{ZnS} = \mu_{Zn} + \mu_S$ $\Delta G_f^{SnS} = \mu_{Sn} + \mu_S$ Maximum of μ_{Ag} or μ_{Cd} for Ag- or Cd-doping under the above constraints, as listed below $\mu_{Ag} = \mu_{Ag}^{metal} \equiv 0$ $\Delta G_f^{CdS} = \mu_{Cd} + \mu_S$
Constrained Cu-poor	$\Delta G_f^{Cu_2ZnSnS_4} = 2\mu_{Cu} + \mu_{Zn} + \mu_{Sn} + 4\mu_S$ $\mu_{Cu} < \mu_{Cu}^{metal} \equiv 0$ $\Delta G_f^{ZnS} = \mu_{Zn} + \mu_S$ $\Delta G_f^{SnS} = \mu_{Sn} + \mu_S$ Maximum of μ_{Ag} or μ_{Cd} for Ag- or Cd-doping under the above constraints, as listed below $\mu_{Ag} = \mu_{Ag}^{metal} \equiv 0$ $\Delta G_f^{CdS} = \mu_{Cd} + \mu_S$
Cu-poor	$\Delta G_f^{Cu_2ZnSnS_4} = 2\mu_{Cu} + \mu_{Zn} + \mu_{Sn} + 4\mu_S$ $\mu_{Cu} < \mu_{Cu}^{metal} \equiv 0$ Maximum of μ_{Ag} or μ_{Cd} for Ag- or Cd-doping under the above constraints, as listed below $\Delta G_f^{Ag_2ZnSnS_4} = 2\mu_{Ag} + \mu_{Zn} + \mu_{Sn} + 4\mu_S$ $\Delta G_f^{CdS} = \mu_{Cd} + \mu_S$
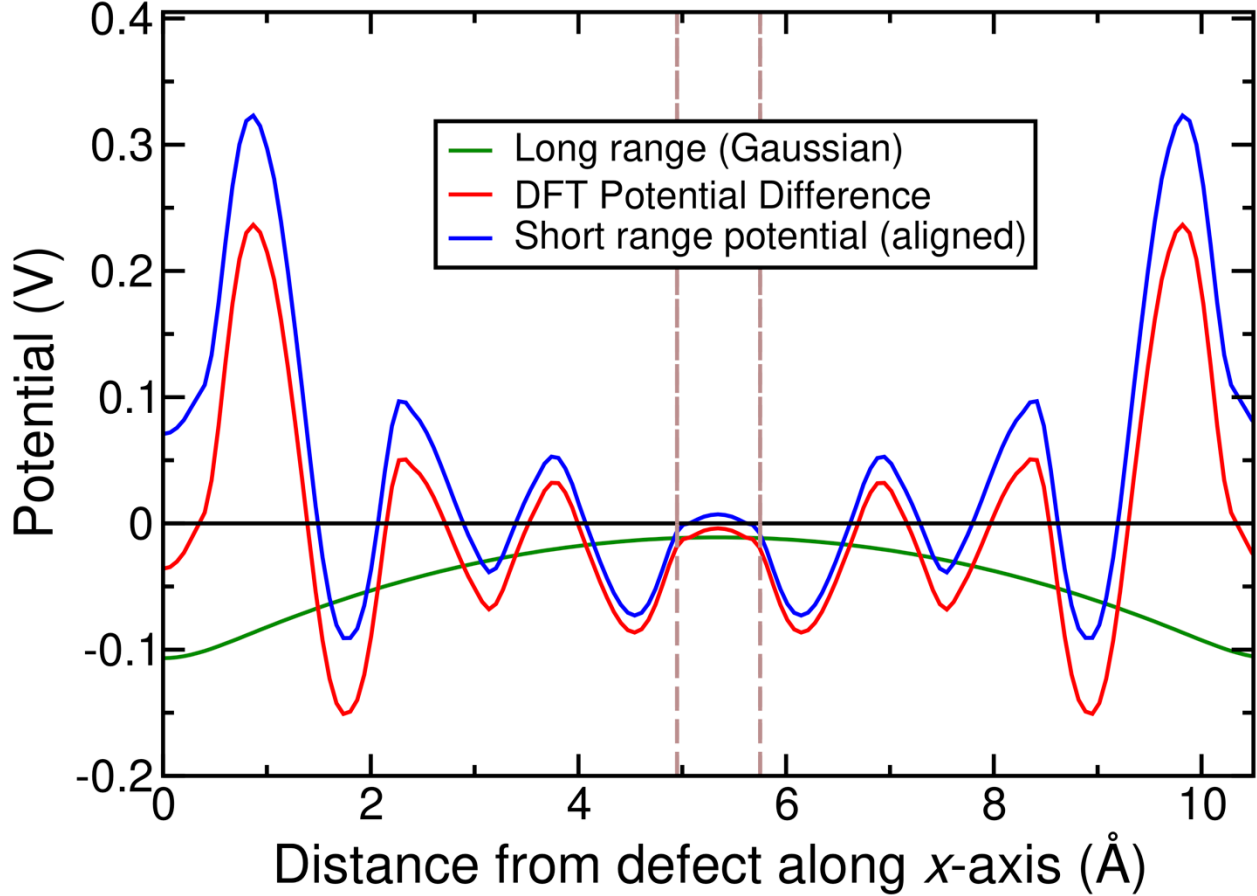
Figure S4: Schematic of the electrostatic correction scheme proposed by Freysoldt *et al.*[10,11] for a positively charged ($q = 1$) Ag_{Cu} defect in kesterite-Cu_2ZnSnS_4. All DFT-based calculations for charged defects in this work use a GGA+U+D functional (see Methods section in the main text). The solid red curve reflects the difference between planar-averaged GGA+U+D-calculated electrostatic potentials of the defective and pristine supercells. The solid green curve signifies the electrostatic interaction between the charged defect and its periodic images obtained by modeling the defect with a Gaussian charge distribution. The solid blue curve reflects the short-range contribution to the electrostatic potential, which is the difference between the DFT-calculated and Gaussian model-based potentials. The region between the dashed brown lines indicates the sampling region, *i.e.*, a spatial region far away from the defect and its periodic image along *x*-axis, nominally used in estimating E_{corr}. The appearance of plateau in the short-range potential within the sampling region indicates that the supercell used ($2 \times 2 \times 2$ of the conventional kesterite structure) is sufficient for converging the charged defect calculation (*i.e.*, the electrostatic potential converges far away from the defect), with a reliable E_{corr} determined. Note that the correction scheme of Freysoldt *et al.* is strictly applicable only for isotropic materials and is merely used in this work to verify the convergence of the electrostatic potential. Instead, we use the anisotropic correction scheme of Kumagai and Oba[12] (**Figure S5**) to obtain values of E_{corr} for all charged defects considered (**Table S7**).
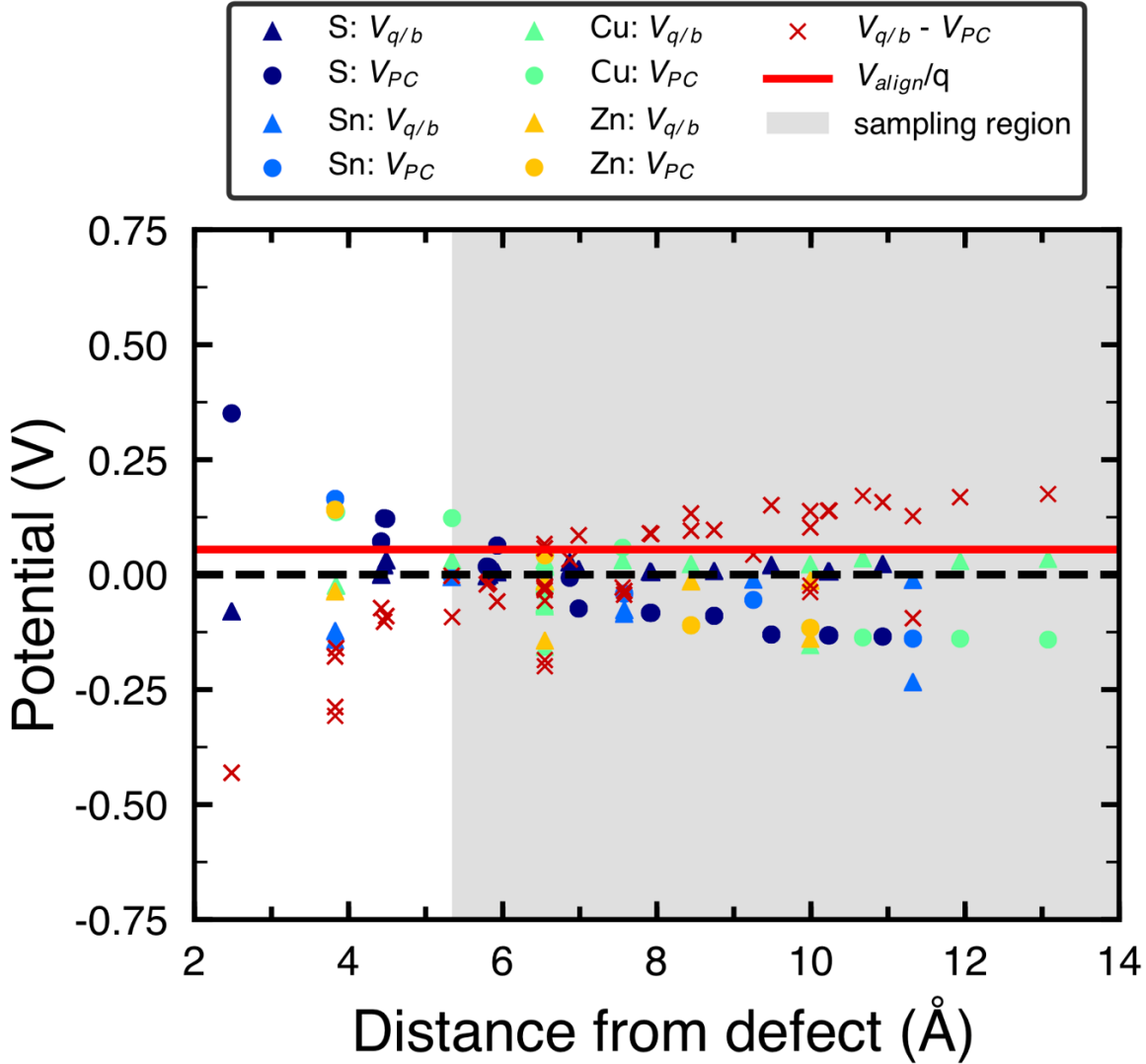
Figure S5: Schematic of the electrostatic correction scheme by Kumagai and Oba[12] for a positively charged ($q = 1$) Ag_{Cu} defect in kesterite-Cu_2ZnSnS_4. All DFT-based calculations for charged defects in this work use a GGA+U+D functional. $V_{q/b}$ (triangles) represent the difference between the DFT-calculated electrostatic potential of the defective (with charge q) and pristine (denoted as "b") supercells at atomic positions corresponding to S (dark blue), Sn (light blue), Cu (green), and Zn (yellow). Analogously, V_{PC} (circles) indicates the electrostatic potential arising from a point-charge model ($q = 1$) of the periodically repeating defect. Thus, V_{PC} has contributions from the charged defect site (modeled as a point-charge, q), its periodic images (point-charges) and the compensating background charge ($-q/V$, V = supercell volume), scaled by the dielectric tensor (**Table 1**). The shaded gray zone reflects the sampling region, encompassing atoms that lie within the Wigner-Seitz cell of Cu_2ZnSnS_4, outside the Wigner-Seitz sphere (radius = 5.34 Å). $V_{q/b} - V_{PC}$ (red crosses) corresponds to the difference between the DFT-calculated and point-charge-model-based electrostatic potential at each atomic site, while the solid red line (V_{align}/q) signifies the average of $V_{q/b} - V_{PC}$ over the sampling region. Finally, the potential alignment correction term ($-q\Delta V$) has a magnitude of $-q * V_{align} = -0.054$ eV, with a net electrostatic correction term (E_{corr}) for the positively charged Ag_{Cu} defect of $+0.071$ eV. Similar calculations are executed for other defect calculations and the corresponding E_{corr} values are given in **Table S7**. We used the python charged defect toolkit[13] for post-processing the charged defect calculations and determining the correction terms.
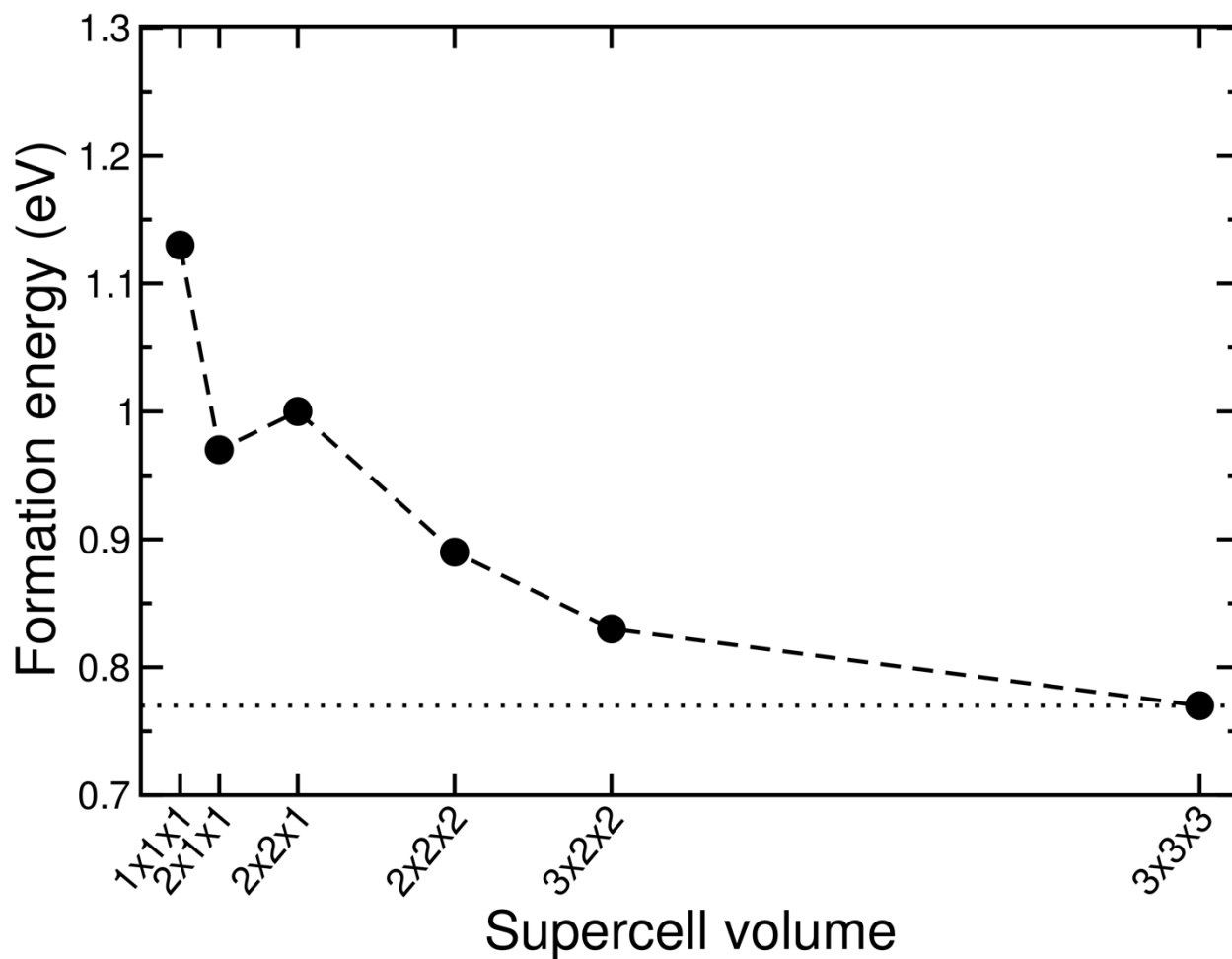
Figure S6: Variation of the formation energy of a charged Ag_{Cu} anti-site ($q = 1$) in kesterite-Cu_2ZnSnS_4, as a function of the supercell size used. $i \times j \times k$ on the horizontal axis indicates the number of replicas of the conventional kesterite structure along the a, b, and c lattice vectors (Figure 1), respectively. The formation energy is converged to within ~0.1 eV at a supercell volume of $2 \times 2 \times 2$, with respect to a significantly larger $3 \times 3 \times 3$ supercell, which is within typical convergence bounds used for charged defect calculations in periodic boundary conditions.[13–15]

Table S7: Values of the point charge (E_{PC}), potential alignment ($-q\Delta V$), and net electrostatic (E_{corr}) correction terms calculated using the charged defect toolkit[13] and then used to correct the formation energies for all charged defects considered in this work.

Defect	Charge	E_{PC} (eV)	$-q\Delta V$ (eV)	E_{corr} (eV)
Ag_{Cu}	+1	+0.126	-0.054	+0.071
	-1		-0.097	+0.029
Ag_{Zn}	+1		-0.081	+0.045
	-1		-0.029	+0.097
Cd_{Cu}	+1		+0.021	+0.147
	-1		-0.115	+0.011
Cd_{Zn}	+1		-0.040	+0.086
	-1		-0.110	+0.016

Table S8: Formation energies of neutral defects, under Cu-poor conditions, calculated using SCAN and GGA+U+D. Both formation energies correspond to low levels of doping Ag or Cd. The disparity in SCAN and GGA+U+D evaluated formation energies for Ag_{Zn} is probably because the negatively charged acceptor state (Ag_{Zn} with $q = -1$) is predicted to be significantly more stable than the neutral Ag_{Zn} by GGA+U+D.

Neutral defect	Formation energy in SCAN (eV)	Formation energy in GGA+U+D (eV)
Ag_{Cu}	0.139	0.161
Ag_{Zn}	0.030	0.369
Cd_{Cu}	1.399	1.615
Cd_{Zn}	0.123	0.131

References

(1)   Kubaschewski, O.; Evans, E. L.; Alcock, C. B. *Metallurgical Thermochemistry*; Pergamon Press: Oxford; New York, 1967.

(2)   Wagman, D. D. *The NBS Tables of Chemical Thermodynamic Properties : Selected Values for Inorganic and C_1 and C_2 Organic Substances in SI Units*; American Chemical Society and the American Institute of Physics for the National Bureau of Standards: New York; Washington, D.C., 1982.

(3)   Guenter, J. R.; Oswald, H. R. Neue Polytype Form von Zinn(IV)-Sulfid. *Naturwissenschaften* **1968**, *55*, 177–177.

(4)   Mitzi, D. B.; Gunawan, O.; Todorov, T. K.; Wang, K.; Guha, S. The Path towards a High-Performance Solution-Processed Kesterite Solar Cell. *Sol. Energy Mater. Sol. Cells* **2011**, *95*, 1421–1436.

(5)   Grimme, S. Semiempirical GGA-Type Density Functional Constructed with a Long-Range Dispersion Correction. *J. Comput. Chem.* **2006**, *27*, 1787–1799.

(6)   Peng, H.; Yang, Z.-H.; Perdew, J. P.; Sun, J. Versatile van Der Waals Density Functional Based on a Meta-Generalized Gradient Approximation. *Phys. Rev. X* **2016**, *6*, 41005.

(7)   Matsushita, H.; Ichikawa, T.; Katsui, A. Structural, Thermodynamical and Optical Properties of Cu2-II-IV-VI4 Quaternary Compounds. *J. Mater. Sci.* **2005**, *40*, 2003–2005.

(8)   Botti, S.; Kammerlander, D.; Marques, M. A. L. Band Structures of Cu2ZnSnS4 and Cu2ZnSnSe4 from Many-Body Methods. *Appl. Phys. Lett.* **2011**, *98*, 241915.

(9)   Inorganic Crystal Structure Database (ICSD) https://www.fiz-karlsruhe.de/en/leistungen/kristallographie/icsd.html.

(10)   Freysoldt, C.; Neugebauer, J.; Van de Walle, C. G. Fully Ab Initio Finite-Size Corrections for Charged-Defect Supercell Calculations. *Phys. Rev. Lett.* **2009**, *102*, 16402.

(11)   Freysoldt, C.; Neugebauer, J.; Van de Walle, C. G. Electrostatic Interactions between Charged Defects in Supercells. *Phys. status solidi* **2011**, *248*, 1067–1076.

(12)   Kumagai, Y.; Oba, F. Electrostatics-Based Finite-Size Corrections for First-Principles Point Defect Calculations. *Phys. Rev. B* **2014**, *89*, 195205.

(13)   Broberg, D.; Medasani, B.; Zimmermann, N. E. R.; Yu, G.; Canning, A.; Haranczyk, M.; Asta, M.; Hautier, G. PyCDT: A Python Toolkit for Modeling Point Defects in Semiconductors and Insulators. *Comput. Phys. Commun.* **2018**, *226*, 165–179.

(14)   Freysoldt, C.; Grabowski, B.; Hickel, T.; Neugebauer, J.; Kresse, G.; Janotti, A.; Van de Walle, C. G. First-Principles Calculations for Point Defects in Solids. *Rev. Mod. Phys.* **2014**, *86*, 253–305.

(15)   Malitckaya, M.; Komsa, H.-P.; Havu, V.; Puska, M. J. First-Principles Modeling of Point Defects and Complexes in Thin-Film Solar-Cell Absorber $CuInSe_2$. *Adv. Electron. Mater.* **2017**, *3*, 1600353.